Characterization of feed channel spacer performance using geometries obtained by X-ray computed tomography

Haaksman, Viktor A.; Siddiqui, Amber; Schellenberg, Carsten; Kidwell, James; Vrouwenvelder, Johannes S.; Picioreanu, Cristian

DOI
10.1016/j.memsci.2016.09.005

Publication date
2017

Document Version
Final published version

Published in
Journal of Membrane Science

Journal of Membrane Science 522 (2017) 124–139

Contents lists available at ScienceDirect

Journal of Membrane Science

journal homepage: www.elsevier.com/locate/memsci

Characterization of feed channel spacer performance using geometries obtained by X-ray computed tomography

Viktor A. Haaksman [a], Amber Siddiqui [b], Carsten Schellenberg [c], James Kidwell [d], Johannes S. Vrouwenvelder [a,b,e], Cristian Picioreanu [a,*]

[a] Department of Biotechnology, Faculty of Applied Sciences, Delft University of Technology, Van der Maasweg 9, 2629 HZ Delft, The Netherlands
[b] King Abdullah University of Science and Technology (KAUST), Water Desalination and Reuse Center (WDRC), Division of Biological and Environmental Science and Engineering (BESE), Thuwal 23955-6900, Saudi Arabia
[c] LANXESS AG, Kennedyplatz 1, 50569 Cologne, Germany
[d] Conwed Plastics, 2810 Weeks Ave SE, Minneapolis 55414, USA
[e] Wetsus, European Centre of Excellence for Sustainable Water Technology, Oostergoweg 9, 8911 MA Leeuwarden, The Netherlands

ARTICLE INFO

Article history:
Received 20 April 2016
Received in revised form
24 July 2016
Accepted 3 September 2016
Available online 5 September 2016

Keywords:
CT scan
Three-dimensional model
Hydrodynamics
CFD
Spiral-wound membrane module

ABSTRACT

Spiral-wound membrane modules used in water treatment for water reuse and desalination make use of spacer meshes for keeping the membrane leaves apart and for enhancing the mass transfer. Computational fluid dynamics (CFD) has gained importance in the design of new spacers with optimized hydrodynamic characteristics, but this requires a precise description of the spacer geometry. This study developed a method to obtain accurate three-dimensional (3-D) geometry representations for any given spacer design from X-ray computed tomography (CT) scans. The method revealed that the filaments of industrial spacers have a highly variable cross-section size and shape, which impact the flow characteristics in the feed channel. The pressure drop and friction factors were calculated from numerical simulations on five commercially available feed spacers used in practice. Model solutions compared well to experimental data measured using a flow cell for average velocities up to 0.2 m/s, as used in industrial reverse osmosis and nanofiltration membrane operations. A newly-proposed spacer geometry with alternating strand thickness was tested, which was found to yield a lower pressure drop while being highly efficient in converting the pumping power into membrane shear. Numerical model solutions using CFD with geometries from CT scans were closer to measurements than those obtained using the traditional circular cross-section strand simplification, indicating that CT scans are very well suitable to approximate real feed spacer geometries. By providing detailed insight on the spacer filament shape, CT scans allow better quantification of local distribution of velocity and shear, possibly leading to more accurate estimations of fouling and concentration polarization.

1. Introduction

Membrane operations are used increasingly for the removal of various contaminants from water. For instance, microfiltration (MF) and ultrafiltration (UF) separate particulate material, while nanofiltration (NF) and reverse osmosis (RO) retain charged solutes. Industrially, the removal of these contaminants in order to produce potable water is performed using spiral-wound membrane modules. Optimisation of the performance of spiral-wound modules has been focussed mainly on the development of membranes [1] and the design of feed channel spacers [2].

Research into feed spacer design concentrates mainly on the effect of the spacer geometry on the hydrodynamics in the spacer-filled channel. Hydrodynamics, in turn, influences all other performance indicators. The spacer geometry determines the power input required to overcome the hydraulic resistance imposed on the flow, which is dominated by form drag of the spacer filaments and losses due to the change in direction of flow [3]. The dissipation of momentum and the resulting flow pattern are linked to the distribution of shear stress on the spacer filaments and membranes. Disruption of the hydrodynamic boundary layer by means of liquid recirculation regions influences the transport of solutes from and of particulate material towards the membranes

* Corresponding author.
E-mail addresses: V.A.Haaksman@tudelft.nl (V.A. Haaksman), Amber.Siddiqui@kaust.edu.sa (A. Siddiqui), Carsten.Schellenberg@lanxess.com (C. Schellenberg), James.Kidwell@conwedplastics.com (J. Kidwell), J.S.Vrouwenvelder@tudelft.nl, Johannes.Vrouwenvelder@kaust.edu.sa, Hans.Vrouwenvelder@wetsus.nl (J.S. Vrouwenvelder), C.Picioreanu@tudelft.nl (C. Picioreanu).

http://dx.doi.org/10.1016/j.memsci.2016.09.005
0376-7388/

[4], which in turn affects scaling [5], biofouling processes and the permeate flux [6,7]. Moreover, these processes are coupled to one another to increasing extent with increasing time of operation [8]. Therefore, all of these phenomena have to be taken into account when optimising the feed spacer design [9].

Numerical modelling is a powerful tool to assess the impact of design parameters on the process performance, for a wide range of operational conditions encountered in spiral-wound modules. Computational fluid dynamics (CFD) coupled to transport of solutes has been employed in various studies to model flow and permeation, trying to find the optimal feed spacer design [2,10]. Ranade and Kumar [11] showed that model solutions obtained using a flat spacer-filled computational domain did not significantly differ from those using a curved domain when studying the hydrodynamics in a spiral-wound module, which had also been shown experimentally by Schock and Miquel [12]. Flat spacer-filled computational domains have been thus used extensively for studying the effect of alignment and shape of spacer strands in two-dimensional (2-D) as well as three-dimensional (3-D) models. Most of the work in 2-D has been conducted on a ladder-type spacer strand configuration, the spacer strands being aligned transversal and axial to the main flow direction. The effect of the ratios between the diameter of cylindrical strands, strand distance and channel height on the (unsteadiness of) fluid flow [3,13] and solute transport [14–16] has been studied extensively. Furthermore, the alignment of cylindrical strands along the channel height has been investigated using various configurations of the transversal strands, namely zig-zag (alternating on top and bottom membranes), fully submerged and all aligned with either top or bottom [13,16,17]. Moreover, these models have been extended to assess the impact of strand size and alignment on scaling and (bio)fouling in reverse osmosis for desalination [5,7,9], and on nutrient removal performance of membrane biofilm reactors (MBfR) [18]. Although mostly cylindrical strands have been considered, other cross-sectional shapes like triangular, squared [19], saw-tooth [20] and elliptical [21] have also been evaluated.

Simulations in 2-D have allowed for fast computation and qualitative assessment of design parameters for ladder-type spacers. However, quantitative evaluations of spacer designs of which the strand geometries are not symmetrical in the direction lateral to the main flow cannot be performed in 2-D. The increasing availability of computational resources (i.e., powerful computers; stable, fast and accurate numerical methods; versatile and user-friendly CFD software) has allowed the study of various feed spacer designs using 3-D models without this limitation. Work in 3-D has been performed for multiple filtration technologies using spiral-wound membrane modules (NF, MF, FO), although most work has been centred around reverse osmosis and ultrafiltration [2]. The increasing availability of 3-D modelling also triggered the design of new, non-conventional feed spacers with strand cross-sections other than circular [11,22]. Furthermore, multi-layer spacers with more than two layers of crossing spacer strands used conventionally [23,24] and spacer designs consisting of unconnected support structures, varying in shape, have been evaluated [25]. These efforts aside, the majority of studies on optimal spacer design remained focussed on the impact of alignment of cylindrical spacer filaments (flow attack angle, α, and internal strand angle, β) and the impact of their dimensions in relation to their mutual distance and channel height on hydrodynamics and solute transport [11,26–33]. Mainly, this is due to their presumed resemblance to designs already used in practice.

While efforts to accurately represent spacer geometries used in practice in 3-D modelling remained limited to the alignment and diameter of cylindrical strands, less work was directed towards the investigation of the shape and tilt of spacer filaments themselves. However, it has been shown using stereo light microscopy, scanning electron microscopy (SEM) [34,35] and optical coherence tomography (OCT) [36] that the filaments from designs used in practice vary in thickness when looking from the top. These strands are thus far from cylindrical, most likely due to the polymer extrusion technique used in manufacturing. Geometries formed by filaments constructed from extruded circles with varying diameter and truncated cones have been used to better represent these physical characteristics [35,37]. Furthermore, Picioreanu et al. [37] reported that, compared to these more realistic representations, model solutions obtained from geometries with cylindrical filaments may overestimate the pressure drop over the computational domain representing the feed channel. Moreover, this approach has been successfully used to compute axial pressure drop, which was in agreement with measurements using a flow cell for a new spacer design produced using 3-D printing [38].

More accurate geometry representations, however, remain crucial when one's goal is to compare results from modelling studies to experimental measurements on commercially available spacer designs. Furthermore, insight in the effect of spacer strand shape may lead to improved spacer designs. A recent study in which CFD results were compared to experiments using particle image velocimetry opted for more accurate 3-D spacer geometry representations [34]. In addition, modelled biofouling on spacer filaments was shown to be more detrimental to the calculated pressure drop than fouling on the membrane [6], underlining the importance of accurate geometry representation for the evaluation of a spacer design.

Compared to other available 3-D imaging methods (e.g., confocal laser scanning microscopy, CLSM, optical coherence tomography, OCT, magnetic resonance imaging, MRI), X-ray computed tomography (CT) provides a series of advantages: it can be used for non-transparent samples, requires little to no sample preparation, has a high spatial resolution, is unaffected by sample surface gloss often encountered with optical methods, allows the presence of metals and the scanning equipment is becoming increasingly available. The CT procedure uses 2-D images acquired at different angles on the sample to reconstruct the actual 3-D object [39].

The aim of this study was to develop a method to obtain accurate 3-D geometry representations for any given spacer design. First, a workflow was developed to construct precise 3-D geometry representations from X-ray computed tomography scans for several commercially available feed spacers. The pressure drop calculated from simulations using CFD was compared to experimental data measured using a flow cell for average effective flow velocities up to 0.2 m/s as used in industrial reverse osmosis membrane operations [8,10] Moreover, the feed spacers were compared based on shape-induced friction, efficiency of membrane shear stress generation compared to the power input and local shear and velocity distributions. Finally, CFD model solutions were compared to results obtained using conventional representations using strands with circular cross-section from literature.

2. Materials and methods

2.1. Spacer types

Five type of spacers, all 34 mil thick ($\sim$863 μm), were analysed in this study (Fig. 1). The first two types are commercially available from Conwed Plastics (Minneapolis USA) (called here *CON-1* and *CON-2*). These have a similar filament shape and an internal strand angle (β) of 90 degrees, but different strand count (i.e., number of strands per unit of length) and a slight difference in strand thickness. Typically, the fibres have a quasi-elliptical section, tilted in respect to the main flow direction (Fig. 1**A, B**). The third spacer

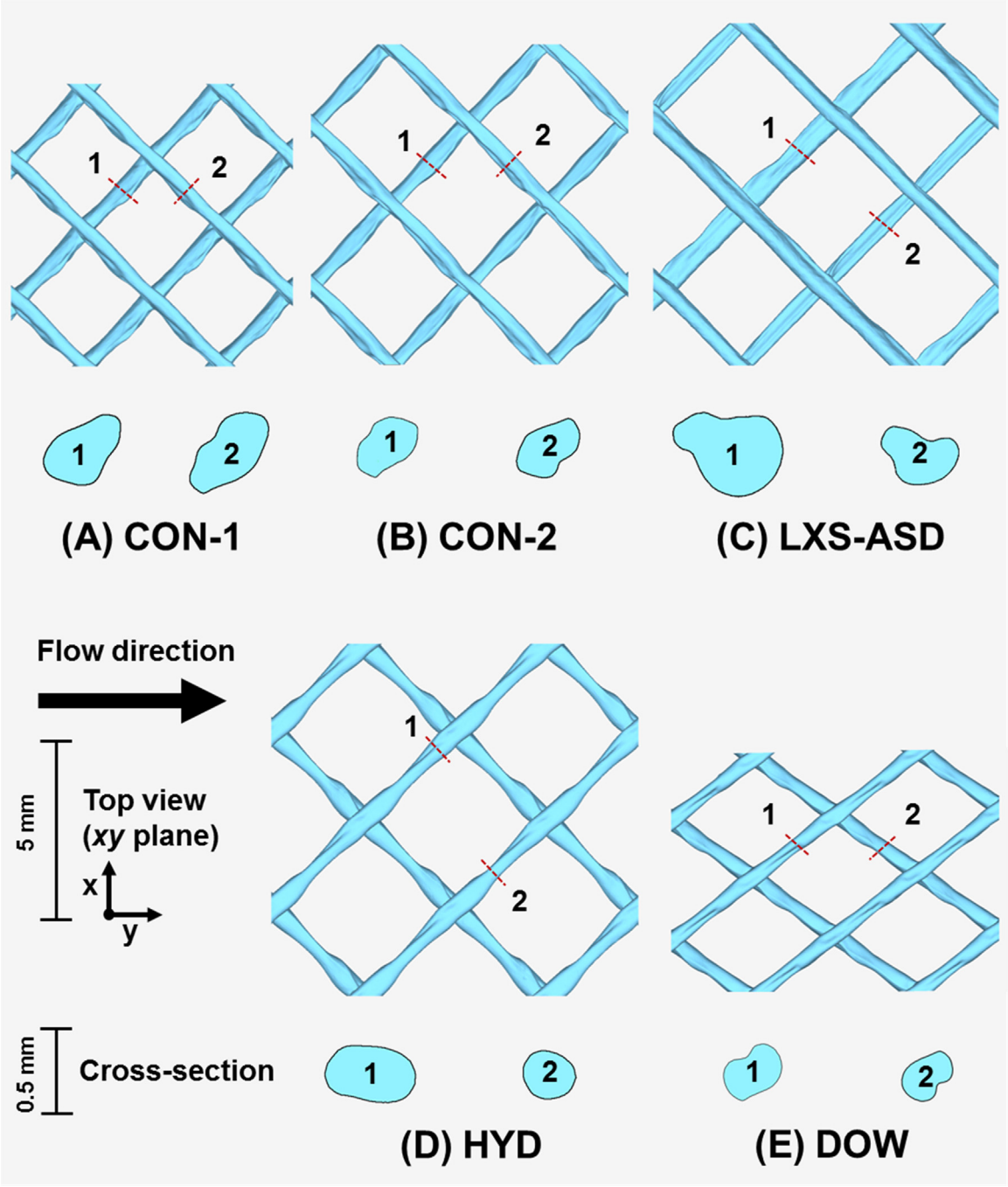

Fig. 1. CT scans of the evaluated feed spacer designs. The top views show the spacers in the *xy*-plane. Two cross-sections normal to the strand axis (90°), at positions along the strands indicated by dashed red lines, are shown below each top view. All images are presented at the same scale (scale bar for top views, 5 mm; for cross-sections, 0.5 mm). The acronyms refer to the spacer manufacturer: Conwed (CON-1, CON-2), LANXESS (LXS-ASD), Hydranautics (HYD) and Dow Chemical (DOW).

was from Hydranautics, also with 90 degrees internal strand angle and elliptical in cross-section, but with profound thinner regions between the strand intersections (called *HYD*) (Fig. 1**D**). A spacer from DOW Chemical with an internal strand angle of 70 degrees was also evaluated (called here *DOW*). This spacer presented strand cross-sections with a small eccentricity (i.e. a small deviation from circular) and almost uniform strand thickness (Fig. 1**E**). Finally, a new spacer design from Lanxess AG (*LXS-ASD*) had alternated strand thickness with the scope of increasing the porosity of the flow channel and therefore reducing the observed pressure drop (Fig. 1**C**). Images of all spacer samples are presented in the Supplementary material (Fig. S1).

2.2. Spacer geometry acquisition and processing

The workflow used to convert the 3-D density information from the CT scanning procedure to a solid shape suitable for calculations using computational fluid dynamics (CFD) is summarized in Fig. 2.

2.2.1. X-ray computed tomography procedure and surface triangulation

Raw CT scans of all selected feed channel spacers were obtained from various sources. For the scan of CON-1, the spacer net was sandwiched between two pieces of expanded polystyrene (Styrofoam) to increase the flatness. However, the other spacers

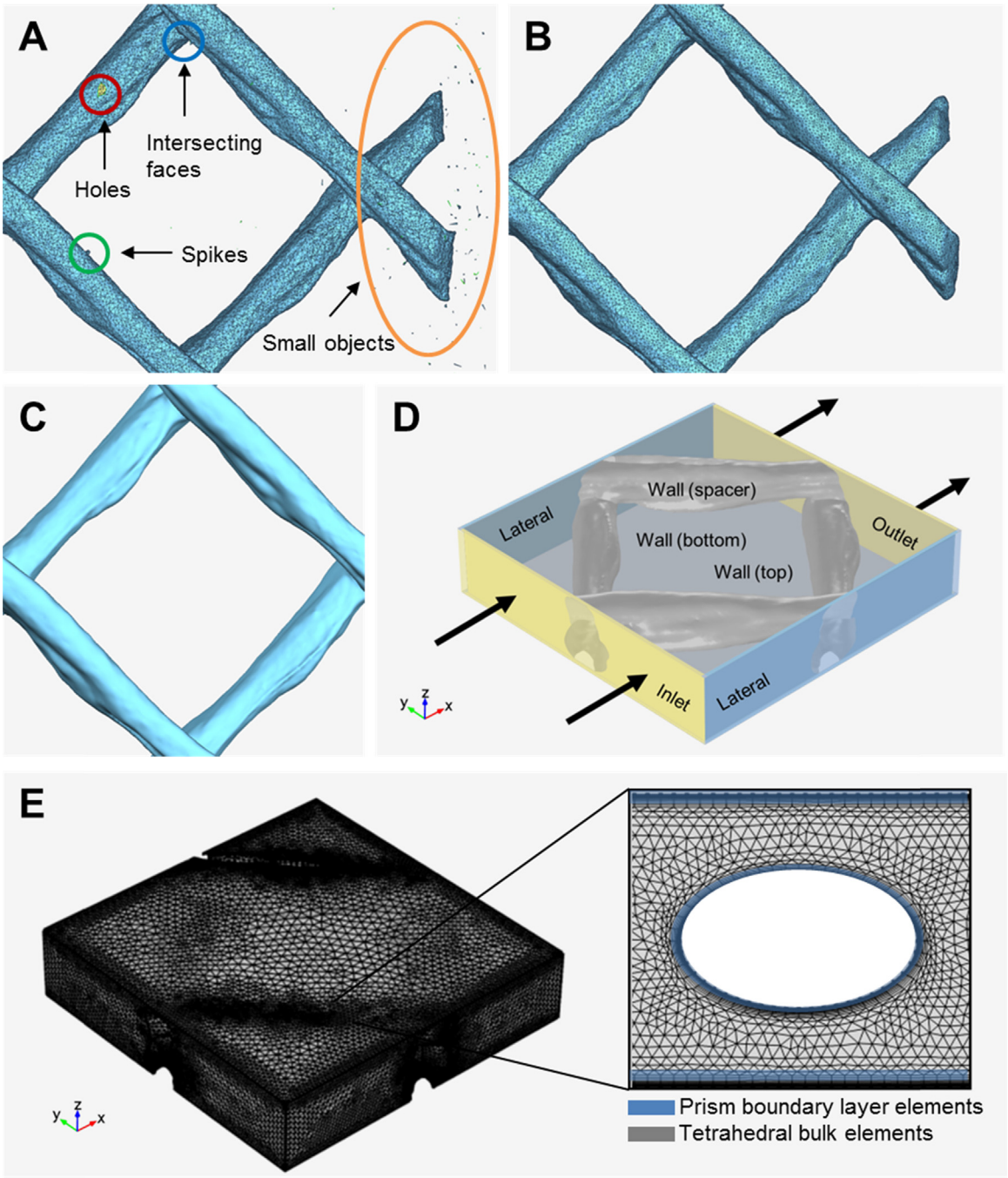

Fig. 2. Overview of the workflow of CT scan processing for CFD modelling for spacer CON-1. (A) Image of an initial three-dimensional surface triangulation containing holes (non-manifoldness), spikes, intersecting surface triangle faces and other small objects (noise). (B) Image of a cleaned triangulated three-dimensional surface. (C) Solid spacer geometry created from surface fitting with non-uniform rational B-spline (NURBS) patches. (D) The computational domain (flow channel) and boundary conditions for CFD. (E) Mesh overview and detail showing boundary layer meshing.

were glued on a support with the plane of the spacer net in vertical position since the rigidity of the small samples was sufficient to ensure the flatness. The scanning procedure used for each spacer design and the properties of the samples that were scanned are summarized in Table 1. The 3-D density information obtained from these scans was subsequently processed to extract only the spacer material by applying a threshold (VGStudio MAX, Volume Graphics GmbH). The surface of the resulting object was then triangulated and the obtained mesh was stored in a common stereolithography file format (STL) [WR1] using the Iso2Mesh [WR2] toolbox for MATLAB (R2014a, MathWorks Inc.). This format contains the positions of vertices and the edges forming the surface triangles, including the normal vector for each triangle. An example of such a mesh is shown in Fig. 2**A**.

2.2.2. *Processing of triangulated surfaces*

The surface triangulation introduces various defects in the 3-D representation of the spacer geometry resulting in holes, sharp peaks, intersecting faces and artefacts on the spacer surface caused by noise in the CT scan (as shown, for example, in Fig. 2**B**). These defects were removed using the open source application MeshLab [WR3], with the goal of creating a manifold (i.e., watertight) geometry. Prior to conversion of the surface mesh to a solid shape, geometry rotation operations were performed with a MATLAB

Table 1
Overview of properties of CT scanned spacer samples and parameters which were used when the CT scan was performed.

Feed channel spacer	CON-1	CON-2	HYD	DOW	LXS-ASD
Sample properties					
Number of strand intersections	17	24	12	17	18
Number of repeating frames	6	9	5	6	3
CT scan procedure					
Voxel size (μm)	15 – 18	7.5	7.5	7.5	7.5
Image acquisitions per rotation	1200	1440	1440	1440	1440
Equipment used	Carl Zeiss Metrotom 800	Phoenix nanotom m, GE Life Sciences	Phoenix nanotom m, GE Life Sciences	Phoenix nanotom m, GE Life Sciences	Phoenix nanotom m, GE Life Sciences

routine in order to align the spacer with the *xy* plane of the used system of coordinates.

2.2.3. Surface fitting and conversion to a solid shape

The netfabb Basic application (3D Systems, Inc.) [WR4] was subsequently used to cut a repeating spacer frame from the manifold surface mesh. A piece slightly larger than required was cut in this operation to avoid alterations in the computational domain due to necessary smoothing of the cutting edges. The resulting piece was imported in GeoMagic Studio (v12.0, 3D Systems, Inc.) and prepared for surface fitting by using the automatic mesh repair functionality, which would smooth the sharp angles between edges introduced upon cutting the surface mesh in the previous step. Then, a surface was fitted onto the mesh using several non-uniform rational B-spline (NURBS) patches based on lines drawn along the important contours of the geometry. The patches were merged to form a single surface, which was subsequently converted to a solid shape (CAD-geometry) for use in the CFD code. An example of a resulting solid geometry is presented in Fig. 2**C**.

2.2.4. Construction of computational domain

Computational domains for modelling hydrodynamics were constructed from solid shapes described in Section 2.2.3. The computational domain was created by imposing a block with sizes in x- and y-directions equal to the dimensions of one (or multiple) repeating spacer frames and with a height of 863.6 μm (34-mil). For each geometry the block was moved along the z-direction to minimize the fluid-filled volume of the channel. Finally, the liquid domain was constructed as the difference between the volumes of the block and spacer (Fig. 2**D**).

2.2.5. Spacer geometry measurements

Distance measurements (i.e. strand intersection thickness, parallel strand distance, strand thickness, etc.) were conducted on the processed triangulated surface mesh. The matrix representation of the spatial position of vertices allowed for faster processing in MATLAB compared to the solid shape of the spacer geometry. Volume measurements were performed on the solid spacer geometries using COMSOL Multiphysics (v5.1, COMSOL Inc., Burlington, MA) and MATLAB through the LiveLink® interface. Thickness measurements were performed using digital callipers. Volumes of physical spacer nets for porosity were calculated from weight measurements based on the material density. The average thickness and porosity of designs with alternating strands were calculated based on the nodes of two strands of the thickest type, assuming that these nodes support the membranes the most and thus determine the feed channel height in spiral-wound membrane modules.

2.2.6. Construction of simplified spacer geometry

Simplified spacer geometries were constructed to mimic the conventional approach of spacer geometry construction for CFD modelling in 2-D as well as 3-D. Measurements on the spacer dimensions have been obtained by light microscopy or scanning electron microscopy [35], always using views from the top of the spacer mesh. Assuming that spacer strands are rotationally symmetric along a central axis, a cylindrical strand with varying diameter could be constructed. The same procedure was applied here, but using instead the top view of the CT scan. A set of Bèzier curves was used to approximate the surface curvature based on these measurements. The simplified solid strand shape was finally created by revolving the Bèzier curves around a central axis, followed by the construction of the channel geometry by multiplying such obtained strand geometry units. All the simplified geometries obtained for spacers HYD, DOW and LXS-ASD are presented in Fig. S2 from the Supplementary material.

2.3. Numerical model

The computational domains constructed from the CT scans were used for three-dimensional CFD calculations. Stationary, laminar flow of an incompressible fluid was assumed (Navier-Stokes with continuity equations):

$$\rho(\mathbf{u}\cdot\nabla)\mathbf{u} + \nabla p = \nabla\cdot(\eta\nabla\mathbf{u}), \quad \nabla\cdot\mathbf{u} = 0 \tag{1}$$

where $\mathbf{u} = (u_x, u_y, u_z)$ denotes the vector of local fluid velocity, p is the pressure, η is the dynamic viscosity of water and ρ is the density of water (30 °C). No-slip boundary conditions were specified for the spacer surface and for top and bottom walls, thus performing calculations without permeate production.

To reduce the computational requirements, while still having a representative computational volume, periodic boundary conditions were applied on one typical spacer frame. The periodic flow conditions were set between the opposite boundaries lateral and axial to main flow direction. Considering that the CT scans contain small deviations in geometry from one repeating spacer frame to the next, the geometry of the opposite faces of the computational domain does not match exactly. To allow the use of periodic boundaries, the computational domain was slightly altered by adding very thin blocks (50 μm thick) on all four faces. Consequently, the periodic boundaries were actually applied on the perfectly matching rectangular faces of opposite blocks. The validity of this approach was tested by additional calculations using a simplified spacer geometry containing identical periodic faces with and without the blocks. Differences in the calculated pressure drop and velocity fields were negligible (less than 0.1%), thereby justifying this approach. A pressure difference between the axial pair of periodic boundaries was driving the flow. The needed

pressure drop to obtain the desired average velocity ($\bar{u}_{set}$) resulted from an additional constraint:

$$\bar{u}_{set} = \bar{u}_x = \int_\Omega u_x dV / \int_\Omega dV \quad (2)$$

where $\bar{u}_x$ is the velocity in the main flow direction, averaged over the whole computational domain Ω.

2.3.1. Model solution and mesh convergence studies

COMSOL Multiphysics 5.1 was used to solve the stationary flow equations by finite element methods. A schematic overview of a computational domain in depicted in Fig. 2**D**. For quantitative comparison with experimental data, it is essential the numerical results are accurately obtained on converged grids (or meshes). A triangular mesh was generated on one face of a pair of periodic boundaries and subsequently copied to the other face of the pair. Tetrahedral elements were then used to mesh the liquid volume of the computational domain with a maximum element size varying per spacer geometry (CON-1: 70 μm, CON-2: 75 μm, HYD: 78 μm, DOW: 66 μm, LXS-ASD: 108 μm). From this tetrahedral mesh, a number of prism shaped boundary layer elements were generated near the no-slip walls (membranes and spacer). The solution was calculated on successively refined meshes until a converged grid was obtained. The degree of convergence was assessed using the Grid Convergence Index (GCI) proposed by Roache [40]. The friction factor f was used as the quantity to assess the convergence. This is equivalent with using the pressure drop as mesh convergence criterion. In the simulated conditions, the GCI was below 10% for all spacers when ten boundary layer mesh elements were generated on the no-slip boundaries. This is considered as sufficient mesh accuracy in CFD [2]. Further refinement of the tetrahedral mesh did not result in an increase in accuracy. Details on the grid refinement and mesh convergence studies can be found in Supplementary Material, Fig. S3.

2.4. Experimental methods

Experimental pressure drop measurements on the spacers under evaluation were performed at cross flow velocities representative for membrane modules in practice [41], using membrane fouling simulators [42] and sensitive differential pressure transmitters [43]. The complete experimental set-up has been described in recent work [38,44]. Feed spacers (thickness of 34 mil) were selected based on earlier studies (e.g., [45]).

Measurements on each spacer type were conducted using the same flow cell with a fixed channel height of 34 mil (863 μm) and inner width and length of 4.0 cm and 20.0 cm, respectively. A mould was used to cut small sheets of spacer to the aforementioned size. Filtered (10 μm pore size) tap water was used for this study with a controlled temperature of 30 °C. Pressure drop measurements were performed in duplicate for a range liquid flow rates between 2 kg/h and 20 kg/h. Flow rates were converted to average velocities $\bar{u}_{eff}$ using the flow channel porosities determined from CT-scans.

2.5. Measures for evaluation of different spacer geometries

2.5.1. Pressure drop

Objective comparison of pressure drop resulted from different spacer designs is crucial for the evaluation of their performance. Experimental measurements and flow simulations on different spacer geometries must be compared based on the same average liquid velocity in the main flow direction $\bar{u}$ corrected for the porosity of the spacer-filled feed channel, ε, such that $\bar{u}_{eff} = \bar{u}/\varepsilon$. The channel porosity (i.e., the volume fraction available for fluid flow) is calculated from $\varepsilon = 1 - V_{sp}/V_{tot}$, where V_{sp} and V_{tot} are the volume of the spacer and the total volume of the channel including the spacer and the liquid, respectively.

2.5.2. Friction factor

When comparing the drag characteristics of different spacers resulting from the shape of the spacer strands and the orientation towards the liquid flow, the Reynolds number, $Re = \rho \bar{u}_{eff} d_h/\eta$, and the Darcy friction factor, $f = 2\Delta p\, d_h/\left(\rho\, l\, \bar{u}_{eff}^2\right)$, were used as proposed by Schock and Miquel [12]. The pressure drop Δp is related to a unit length of flow channel, l. Various definitions for the characteristic length scale of the flow in spacer-filled channels and 3-D simulations have been proposed, which either use only the channel height, h, [4] or the strand diameter d_S [29], thus assuming on average cylindrical strands. However, the wetted area A_w (spacer and all other walls) and the shape of the spacer strands would also influence the friction factor. Therefore, the definition of a hydraulic diameter d_h proposed by Schock and Miquel [12] is the most widely used [2] and allows for analysis of spacer designs without *a priori* assumptions on the strand shape.

$$d_h = \frac{4\,(V_{tot} - V_{sp})}{A_w} = \frac{4\,V_{tot}\varepsilon}{A_m + A_{sp}} \quad (3)$$

This hydraulic diameter takes into account the porosity of the spacer-filled channel, ε, the spacer surface area, A_{sp} and the membrane surface area, A_m. The advantage of CT scans is that it allows an accurate calculation of the spacer surface area and volume without assuming a particular shape of the strands.

2.5.3. Membrane shear stress generated per power input

Besides the pressure drop, the solute (e.g., salt) transport and (bio)fouling are important in the operation of industrial reverse osmosis modules and these are impacted by shear [26,32,35]. Therefore, feed spacer performance was also assessed in terms of the energy loss resulting from the form drag through flow around the spacer strands in a feed channel and shear stress on the membrane surface. The influence of the strand shape (i.e. regardless of the dimensions) was assessed by getting a modified friction factor (f_{mod}) proposed by Santos et al. [22] as a function of the Power number, which allowed comparison of different spacer designs for the same power input. The Power number, Pn, was defined as $Pn = Re^3 f$. The modified friction factor is a function of shear at the membrane, $f_{mod} = \tau_m\left(d_h^2\,\rho/\mu^2\right)$, where τ_m is the shear averaged over the whole membrane area. The f_{mod} should ideally be maximized for a given power input.

2.5.4. Membrane shear stress efficiency for a constant flow rate

Another operational mode of spiral-wound membrane modules is operation using a constant feed flow rate. Therefore, the shear stress on the membrane per unit of pressure difference for a spacer design as a whole was analysed for a fixed average velocity $\bar{u}_{eff}$ to assess the level of hydrodynamic boundary layer disruption on the membrane per amount of momentum dissipated. To be able to compare correctly different spacer designs, the dimensionless quantity $f_p = \left(\tau_m/\Delta p\right)\left(A_m/A_{axial}\right)$ was used.

A_{axial} is the cross-sectional area of the computational domain perpendicular to the main flow direction.

2.5.5. Strand eccentricity

The strand eccentricity for a spacer of a certain cross-section was calculated by $e = \sqrt{1 - b^2/a^2}$, where e is the eccentricity, b the shortest semi-axis and a the longest semi-axis. A circular cross-section yields an eccentricity of 0, while e increases asymptotically towards 1 for increasing eccentricity. Lengths a and b define the ellipse circumscribing a cross-section of spacer strand with the

smallest circumference. Average eccentricity of the strand was determined by averaging the eccentricities of 20 cross-sections.

3. Results

3.1. Geometric characteristics of feed channel spacers from CT scans

Visual inspection of the CT scans of the spacers under study reveals a variety of geometric features, hardly observable by previously used microscopic methods. Ridges, valleys and varying strand thickness in all three dimensions are apparent for all five feed channel spacer designs, features sometimes generated by twisted strands between fibres intersections. The CT scans clearly revealed that the cross sections of the fibres are not rotationally symmetric (see Fig. 1). This means that the spacer strand orientation against the flow becomes important, unlike in previous spacer representations where the cross-sections were circular [34,35,37].

Quantitative geometry measures were extracted from the CT scans for each spacer design. In the following, we annotate with an asterisk (*) the measured quantities that were changed in the model due to the fixed height of the experimental flow channel (h=863 μm). The average thickness of strand nodes, h^*, and the average parallel strand distance, L_{sp}, were measured to validate the dimensions of the CT scan. The volumes, V^*_{sp}, and surface areas, A^*_{sp}, of several repeating elements in each spacer geometry were calculated from the CT scans. From these, the porosity of the flow channel corresponding to each spacer, ε^*, and the specific surface area, A^*_{sp}/V^*_{sp}, could be calculated. Calculated and physically measured values are listed in Table 2 for comparison.

The deviation of the average spacer thickness calculated based on the CT scans from the thickness measured using digital callipers varied per spacer design. The differences may occur either due to the small force exerted by callipers on the spacer net (which may slightly deform, e.g., LXS-ASD). Additional sources of inaccuracy could be the variation in spacer sheet thickness between different production batches and that different sheets had been used for CT scanning than for the physical measurements. Despite these possible sources of error, the calculated average spacer thickness was in good agreement with the measured thickness for spacers CON-1, CON-2, HYD and DOW. Moreover, parallel strand distance calculations based on the CT scan matched well the measured values for each spacer geometry (Table 2). Based on these findings, the dimensions of the CT scans were concluded to be valid.

Flow channel porosities calculated using the CT scan compare well to those based on weight measurements. Because of higher accuracy, the CT scan porosities were further used in this study. CON-1, CON-2 and DOW have the lowest porosity (0.856, 0.859 and 0.862), while HYD and LXS-ASD have the largest (0.893 and 0.897). Accurate channel porosity determination is important for calculating the average liquid velocity and, subsequently, for comparing hydraulic characteristics (e.g. pressure drop) of different spacer designs.

3.1.1. Impact of resolution on geometry characteristics

The effect of the resolution at which a CT scan was acquired on the geometry characteristics of the 3-D representations was investigated by comparing the results of different resolutions. Characteristics for spacers CON-2 and DOW extracted from CT scans acquired with a resolution of 7.5 μm and 60–80 μm, respectively, are listed in Table 3. Comparison with measurements

Table 2
Overview of geometric characteristics of spacer designs.

Spacer characteristics	CON-1	CON-2	HYD	DOW[a]	LXS-ASD[b]
Measurements					
Spacer thickness, h^*					
– From CT scan (μm)	852 ± 11	822 ± 6	816 ± 6	803 ± 9	903 ± 7
– From calliper measurement (μm)	847 ± 24	825 ± 9	820 ± 22	806 ± 14	830 ± 15
Average parallel strand distance, L_{sp}					
– From CT scan (mm)	2.28	2.65	2.91	2.34	3.11/2.47
– From calliper measurements (mm)	2.26	2.67	2.85	2.43	2.95/2.63
Average strand thickness, d_{sp} (μm)	50	59	50	43/48	65/50
– Maximum (μm)	56	67	62	48/52	74/53
– Minimum (μm)	42	47	35	38/42	58/46
Average strand eccentricity[c]	0.45	0.62	0.59	0.52/0.43	0.67/0.68
– Maximum	0.63	0.79	0.75	0.64/0.45	0.76/0.74
– Minimum	0.20	0.47	0.42	0.20/0.41	0.46/0.57
Inner strand angle, β (°)	90	90	90	70	90
Specific spacer surface area, A^*_{sp}/V^*_{sp}(m^2/m^3)	8828 ± 87	8413 ± 44	8927 ± 2	9083 ± 27	9490
Flow channel porosity, ε^*[d]					
– From CT scan	0.856 ± 0.002	0.859 ± 0.001	0.893 ± 0.001	0.862 ± 0.002	0.897 ± 0.001
– From density based calculation	0.861 ± 0.012	0.863 ± 0.007	0.892 ± 0.005	0.878 ± 0.009	0.879 ± 0.002
Numerical model					
Dimensions					
– Flow channel height, h (μm)	863	863	863	863	863
– Spacer frame axial length, L_x (mm)	3.90	4.47	4.93	4.70	9.63
– Spacer frame lateral length, L_y (mm)	3.90	4.56	4.73	3.42	9.53
Mesh length over channel height, L_m/h	4.5	5.2	5.6	5.4	5.6
Specific surface area A_{sp}/V_{sp} (m^2/m^3)	8811	8422	8973	9052	9537
Flow channel porosity, ε[d]	0.855	0.866	0.893	0.873	0.893
Hydraulic diameter, d_h (mm)	0.97	1.01	1.09	1.01	1.07

[a] Thickness calculated based on top view of a spacer. For spacer DOW, the pair of numbers represents the values for the respective top and bottom filaments.
[b] For spacer LXS-ASD, the pair of numbers represents the values for the respective alternating strands.
[c] Average eccentricity was calculated by maximizing the difference between two orthogonal thicknesses.
[d] Estimated feed channel porosity using a certain spacer in spiral-wound modules differs from the porosity of the channel in the numerical model and experimental set-up due to the imposed channel height of 863 μm in the latter case.

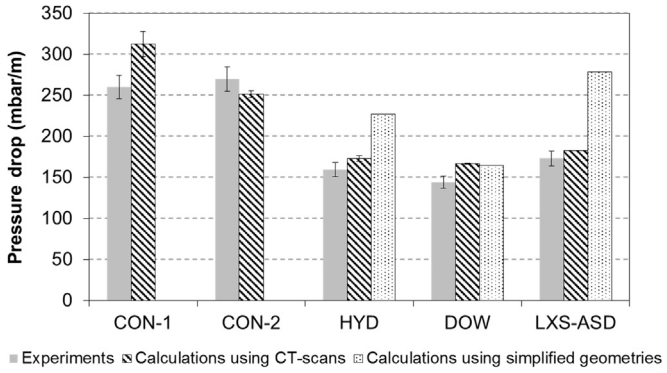

Fig. 3. Comparison of measured and calculated pressure drop per metre, for all spacer designs, at $\bar{u}_{eff}$ =0.163 m/s. Grey bars: experimental measurements; error bars represent the standard deviation between determinations (n=3). Hatched bars: model results with spacer geometry from CT scans; errors bars represent standard deviation between calculations using different spacer frames from the CT scan (n=5). Dotted bars: model results for simplified spacer geometries.

conducted using digital callipers clearly show that a scanning resolution of 60–80 μm results in a too coarse geometry representation, while the scan acquired with a resolution of 7.5 μm was in close agreement with the measurements. The specific spacer surface area (A^*_{sp}/V^*_{sp}) was found to be smaller using a higher resolution of 7.5 μm compared to 60–80 μm, indicating that the spacer volume is underestimated using the coarse CT scan. The intersection thickness was considered to be the most useful quality measure for CT scans of feed spacers, since too coarse CT scans yielded geometries with significantly smaller thickness compared to the measured data. Therefore, the resolution of 7.5 μm was preferred for obtaining digital geometry representations of feed channel spacers.

3.2. Hydraulic characterization

3.2.1. Pressure drop measurements compared to model solutions using CT scans

Measured pressure drop data at a velocity commonly used in practice, $\bar{u}_{eff}$ =0.163 m/s [8], are shown in Fig. 3. A similar pressure drop was measured for spacer designs HYD (159 ± 9 mbar/m), DOW (144 ± 7 mbar/m) and LXS-ASD (173 ± 9 mbar/m), performing the best of the evaluated spacers, while higher pressure drop was measured for CON-1 (260 ± 14 mbar/m) and CON-2 (270 ± 15 mbar/m). These differences may be attributed to several factors. First, spacers CON-1 and CON-2 both have a lower channel porosity compared to HYD, DOW and LXS-ASD. Second, the quasi-elliptical strand section of CON-1 and CON-2 (see average eccentricity of spacer strands in Table 2) has a flow attack angle of 20° due to the strand tilt, leading to more drag, compared with the elliptical section of HYD, which is aligned with the flow (Fig. 1). Although strands of DOW are relatively circular in cross-sections, this spacer design has a smaller angle between strands in flow direction (β=70°), which lowers the hydraulic resistance and results in a lower pressure drop, comparable to that from spacers with more eccentric strands like HYD and LXS-ASD (β=90°). Even though both strands of LXS-ASD are on average thicker those of HYD, the alternating strand configuration and the more eccentric strand shape of LXS-ASD yields a similar pressure drop compared to HYD. The non-rotationally symmetric strand sections and strand tilt with respect to the flow are thus important characteristics influencing the pressure drop (Table 3).

Numerical calculations using CFD were performed on spacer-filled channels with a fixed channel height of 34 mil (h=863.6 μm). A representative repeating frame from the CT scan of each spacer design was used to construct the computational domain. For statistical treatment, the calculations were performed on several single frames from the same spacer scan. The pressure drop calculated for spacers CON-2, HYD and LXS-ASD at $\bar{u}_{eff}$ =0.163 m/s was in agreement with the physical measurements (average differences of −7%, +10% and +6% respectively), while the pressure drop for spacers CON-1 and DOW were overestimated with respectively 17% and 16% (Fig. 3).

Pressure drop measurements were performed for average effective velocities up to $\bar{u}_{eff}$ =0.2 m/s (Fig. 4). Quadratic dependencies of the measured pressure drop on the average effective velocity were found, following Bernoulli's law. The level of agreement between the model solutions and the experimental measurements differs per spacer. The model solutions of the CT scanned spacer geometries yielded a slight over- (CON-1 and DOW) or underestimation in the upper region of the velocity range (CON-2) of the pressure drop compared to the experimental measurements, while a good agreement or a slight underestimation was obtained for spacers (HYD and LXS-ASD).

The observed differences between measured and calculated pressure drop can be attributed to different reasons. Deviations in slope between experimental and model results in the upper region of effective velocity range (up to 0.2 m/s), most evident in the graph representing spacer CON-2 in Fig. 4, could indicate the transition from steady to unsteady flow, which would invalidate the assumption of steady laminar flow for these velocities. Furthermore, the average thickness measured for spacers CON-1 and LXS-ASD (h^*) was very close to the channel height of the flow cell and filaments of all spacers are irregularly shaped. Therefore, part of the spacer exceeding the imposed channel height (h) was cut off when constructing the computational domain. If the spacer sheet is too thick at some locations, when used in a flow cell, it would deform instead, resulting in a mismatch between the scanned geometry and the actual geometry in the flow cell and thereby different flow patterns.

3.2.2. Friction from strand shape and orientation

The friction factor f was used to assess the impact of the strand shape and orientation on the hydraulic performance of a particular spacer design. For comparison of different spacers, the friction factor

Table 3
Geometry characteristics of spacer CON-2 and DOW extracted from CT scans acquired with different resolutions compared to measurements using digital callipers.

Spacer	CON-2			DOW[a]		
Method	Measured	CT scan (7.5 μm)	CT scan (60 – 80 μm)	Measured	CT scan (7.5 μm)	CT scan (60 – 80 μm)
Intersection thickness (μm)	825 ± 9	822 ± 6	776 ± 13	806 ± 14	803 ± 9	749 ± 16
Parallel strand distance (mm)	2.67	2.65	2.71	2.43	2.34	2.31
Porosity	0.863 ± 0.007	0.859 ± 0.001	0.869 ± 0.002	0.878 ± 0.009	0.862 ± 0.002	0.877 ± 0.001
Strand thickness (μm)	–	59	49	–	43 / 48	46
Specific spacer surface area (m^2/m^3)	–	8413 ± 44	9117 ± 118	–	9083 ± 27	9897 ± 51

[a] The CT scan with a resolution of 7.5 μm revealed a slight difference in thickness between the bottom and top strand of the sheet of spacer DOW (or vice-versa).

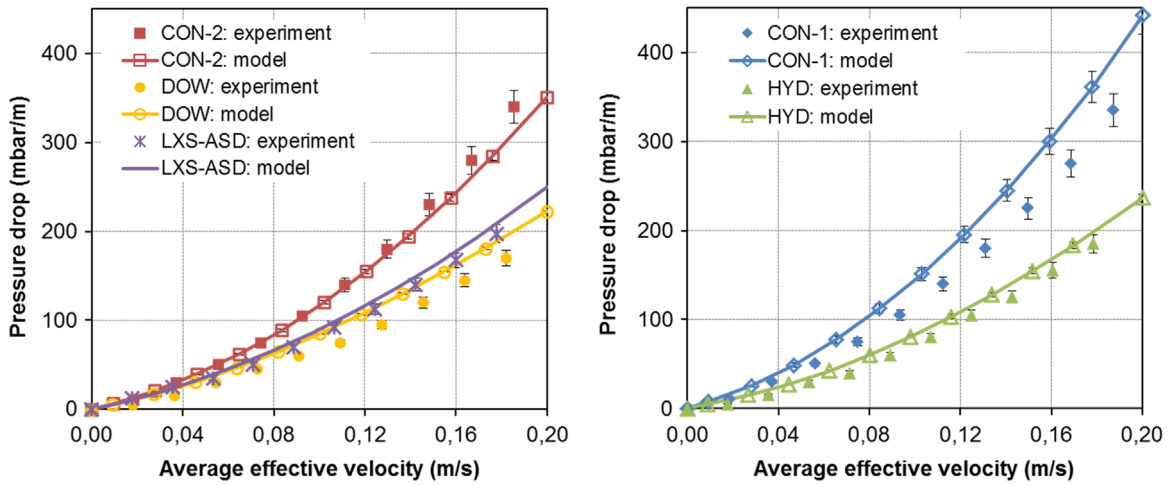

Fig. 4. Pressure drop per metre at different average effective velocities $\bar{u}_{eff}$ up to 0.2 m/s, for all spacer designs. Symbols: experimental measurements; lines: average model data computed using CT scans. Error bars for experimental data represent standard deviation of triplicate measurements for each spacer. Error bars in model results originate from model solutions for different frames of each spacer design (n=5).

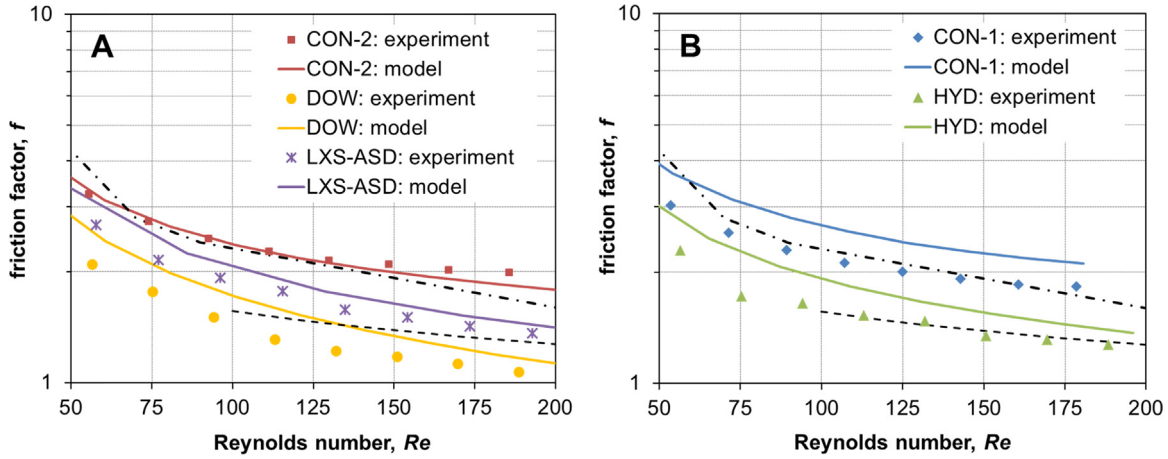

Fig. 5. (A and B) Darcy friction factor function of Reynolds number, calculated from pressure drop measurements and model solutions, for all spacer designs. Symbols: experimental measurements; Solid lines: average model data computed using CT scans; Dashed lines: correlation proposed by Schock and Miquel (1987) for $100 < Re < 1000$, $f = 6.23 \cdot Re^{-0.3}$; Dash-dot lines: numerical data from Fimbres-Weihs and Wiley (2007) for geometry with cylindrical strands ($L_m/h=4$, $d_{sp}/h=0.5$, $\alpha=45°$, $\beta=90°$).

was expressed as a function of the Reynolds number for an average effective velocity up to 0.2 m/s ($50 < Re < 200$). Results for both experimental measurements and model solutions are shown in Fig. 5, where they are also compared with the correlation $f=6.23 \cdot Re^{-0.3}$ ($100 < Re < 1000$) proposed by Schock and Miquel [12].

Both pressure drop and friction factor are providing the same quantitative basis for comparing the model with experiments by using the same d_h and ε based on the CT scans (see Table 2). However, the friction factor, being a dimensionless measure, does provide insight on the drag due to the shape of a certain spacer design regardless of its physical dimensions. A more detailed comparison of experimental and model results seems to indicate that the decrease in f with Re in the interval $125 < Re < 200$ levels off to a larger extent for the experimental data than for the numerical results obtained with steady laminar flow (this is particularly visible for spacer CON-2 in Fig. 5**A**). The onset of unsteady flow phenomena could provide an explanation for this systematic observation, which has been reported in other modelling studies for the Reynolds numbers studied here [2].

The shapes of spacers CON-1 and CON-2 generate more drag compared with the spacers HYD and LXS-ASD (all having the same inner strand angle). In spite of having similar excentricity, the higher f for CON-1 and CON-2 can be attributed to smaller hydraulic diameters and, moreover, the strands are tilted with respect to the direction of the flow (the largest ellipse semiaxis is at an angle of approximately 20° with the main flow direction). The DOW spacer has the lowest friction factor of all spacer designs. Although the strands of DOW are close to cylindrical and the hydraulic diameter is smaller compared to HYD and LXS-ASD, the smaller friction factor results from the smaller inner strand angle (70° compared to 90°). LXS-ASD, even though it has the largest specific surface area of all spacers under study, it also increases the feed channel porosity due to the relatively thin alternating strand leading to a relatively low pressure drop and friction factor.

3.2.3. *Shear at the membrane and power input*

Although pressure drop is important to evaluate the performance of a particular spacer design, the mass transfer and the fouling potential are also critical characteristics, both depending on shear. Contour maps of the bottom membrane shear stress from model solutions for an average effective velocity of 0.163 m/s are presented in Fig. 6. Comparison of the shear distribution of spacers CON-1 (Fig. 6**A**) and CON-2 (Fig. 6**B**) both yielded a maximum shear stress of 8.3 N/m^2 and a similar pattern consisting of high shear stress in the regions below the top filaments. CON-1 presents a curved region of relatively high shear along the middle

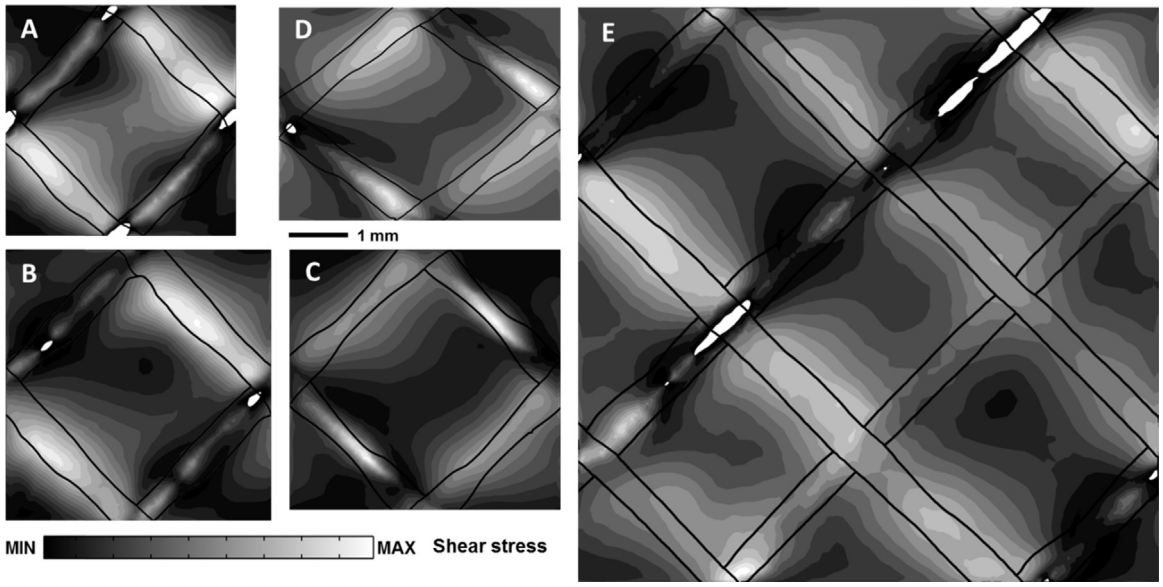

Fig. 6. Contours of shear stress on membranes for all spacers at an average effective velocity of 0.163 m/s (A: CON-1, B: CON-2, C: HYD, D: DOW, E: LXS-ASD. The grey scale is relative to the maximum membrane shear stress of each spacer (A: 8.3 N/m^2, B: 8.3 N/m^2, C: 8.6 N/m^2, D: 6.9 N/m^2, E: 6.3 N/m^2). Overlaid black lines represent the outlines of the spacer geometry.

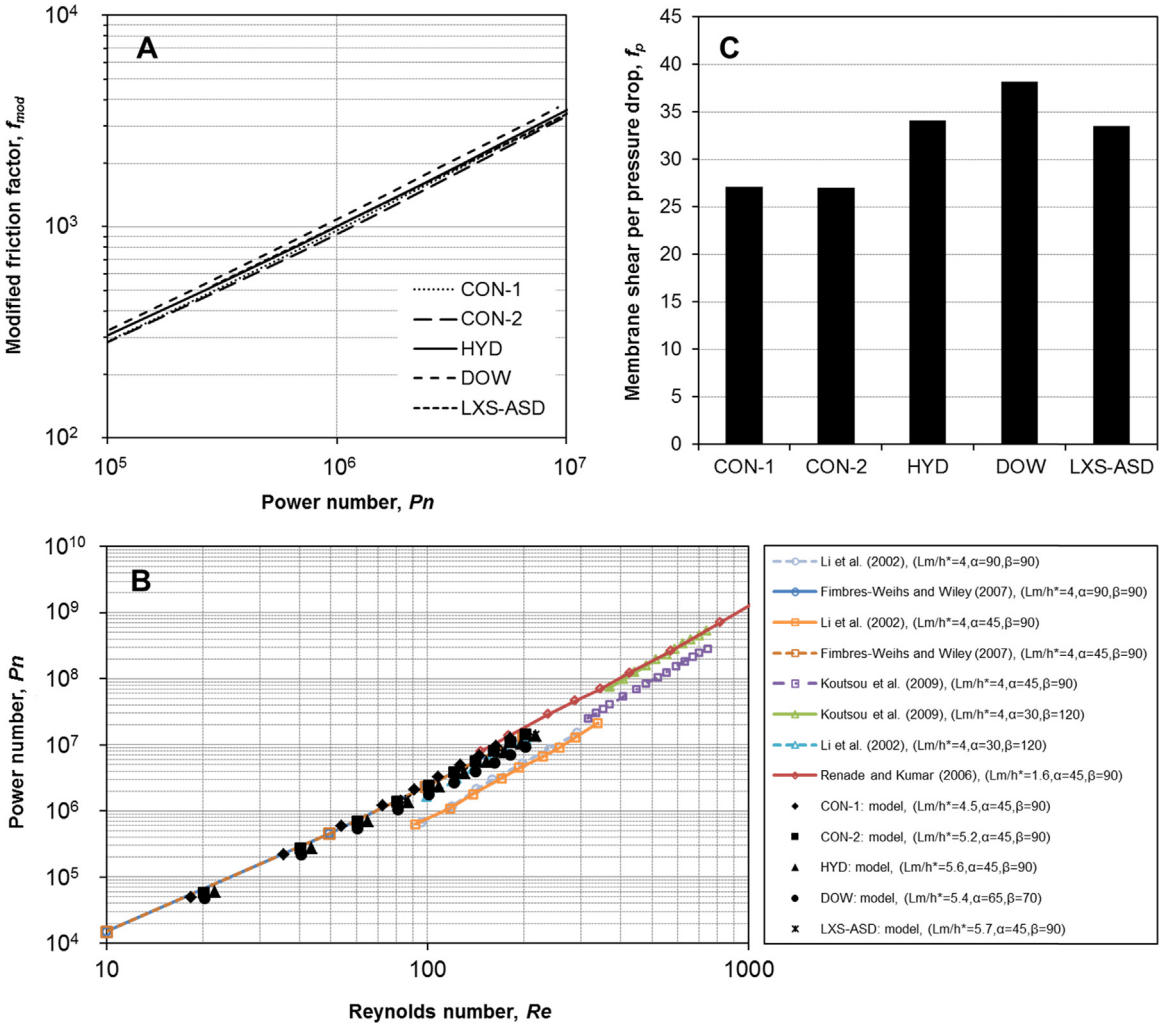

Fig. 7. (A) Modified friction factor (incorporating the average shear stress on both membranes) function of the Power number (Re^3f) in CFD simulations for all spacer designs. (B) The Power number as function of the Reynolds number for all spacers compared to results obtained using cylindrical strands in previous work (figure adapted from Fimbres-Weihs and Wiley [2]. (C) Calculated average shear rate on the membrane surfaces (top and bottom) per unit of pressure drop for an average effective velocity of 0.163 m/s. The average membrane shear rates were 3556, 2919, 2579, 2745 and 2664 1/s from left to right.

of the mesh frame, while this pattern is less pronounced for CON-2 probably due to its larger mesh length. The maximum shear stress for spacer HYD (Fig. 6**C**) was similar, 8.6 N/m^2, but the highest shear stress was localized below the thinnest part of the bottom filament. A distinct region of low shear was located on a line through the middle of the frame. The same high shear regions below the bottom filaments were observed for spacer DOW (Fig. 6**D**), although the maximum shear stress was lower (6.7 N/m^2). Spacers CON-2, HYD and DOW all present a region of low shear downstream of strand intersections, while for CON-1 this is less pronounced. Finally, the model solution for LXS-ASD (Fig. 6**E**) yielded a maximum shear stress of 6.3 N/m^2.

Spacer designs can be optimized on their ability to disrupt (with a minimum power input) the hydrodynamic boundary layer and increase the shear on the membrane, which would be beneficial for the mass transfer. To this aim, dimensionless relations were used, which correlate the Power number ($Re^3 f$) to a modified friction factor incorporating the average shear on the membrane (f_{mod}) introduced by Santos et al. [22]. The CFD calculations revealed that the spread in performance between the spacers is small over the whole range of Reynolds numbers evaluated (Fig. 7**A**). A similar analysis was performed for the industrially-relevant average effective velocity of 0.16 m/s to estimate the shear generated on the membrane per unit of pressure drop, f_p (Fig. 7**C**). The simulations revealed in more detail that the best performance in terms of shear obtained per pressure drop at this average effective velocity is delivered by spacer DOW, followed by LXS-ASD and HYD. Therefore, they exhibited the highest efficiency in converting the pumping power into membrane shear.

3.2.4. *Spatial velocity distribution*

Velocity fields computed for spacers CON-1, DOW and LXS-ASD at three heights in the flow channel are depicted in Fig. 8, showing one full repeating frame for all designs for an average effective velocity of 0.163 m/s. The flow pattern near the membranes (at z=216 and 648 μm) for spacers CON-1 and DOW is mostly guided by the spacer strand orientation in the bottom and top slice, and aligns with the main flow direction in the middle of the channel (z=432 μm). The change in flow direction occurs when the liquid passes above or below spacer strands, which can be concluded from the two axial slices shown in Fig. 8. Noticeably, spacer CON-1 leads to vortex formation and higher velocities, probably due to the tilted strands, which may also explain the larger pressure drop obtained in this case. Qualitatively similar flow patterns were observed for spacers CON-2 and HYD, as shown in Fig. S4.

The extent to which the direction of flow is determined by the strand orientations differs for the spacer with alternating strand thickness (LXS-ASD, Fig. 8**A–E**). The thickest strands – supporting and thereby also imprinting the membranes – occupy a larger fraction of the available channel height and direct the flow to the largest extent. The thinnest strands and their intersections are mostly submerged in the channel, thus imposing less obstruction to liquid flow and channelling the flow to a smaller extent. Furthermore, the magnitude of the velocity component in the main flow direction $|u_x|^2$ and the total velocity vector magnitude $|\mathbf{u}|^2$ were averaged along the channel height in the middle of two consecutive frames (Fig. 8 shows with red circles the positions where velocities were averaged). The ratio $|u_x|^2/|\mathbf{u}|^2$ was 0.80 when preceding a thick-strand intersection (open red circle in Fig. 8**C**) and 0.96 when preceding a thin strand intersection (filled red circle in Fig. 8**C**). This difference demonstrates that the thickest strands guide the flow to the largest extent.

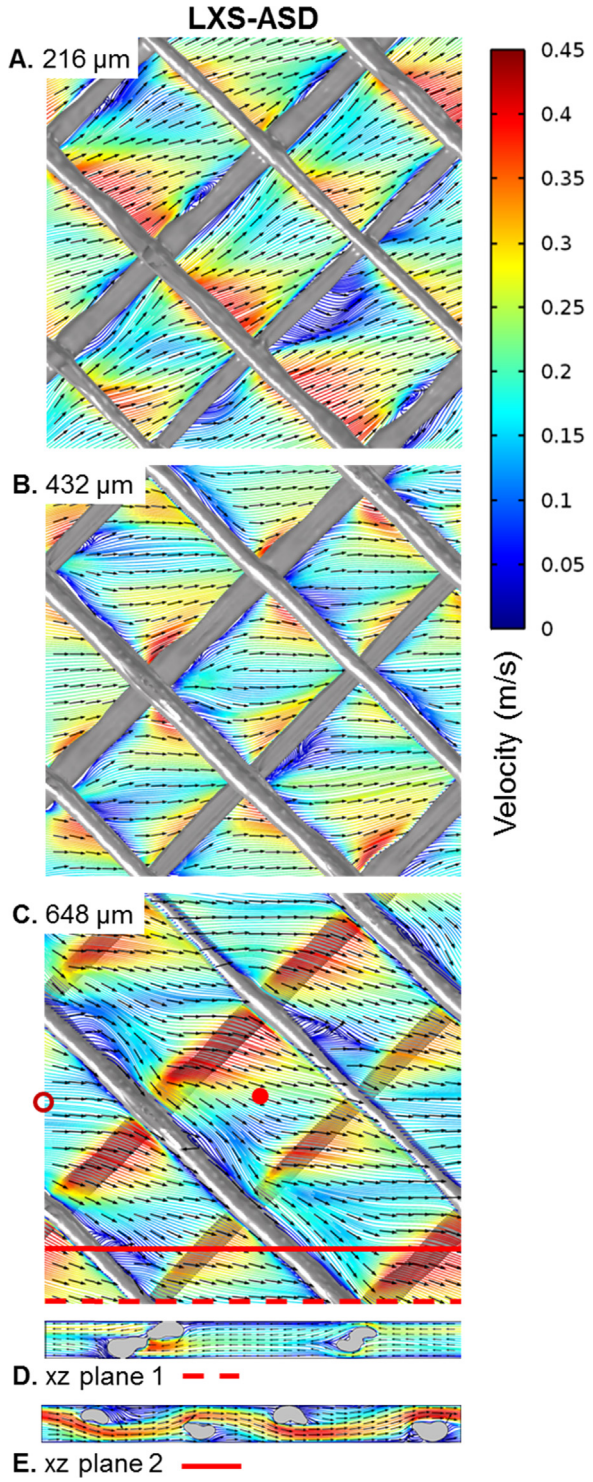

Fig. 8. Flow fields calculated using spacer geometries from CT scan for LXS-ASD at average effective velocity 0.163 m/s. (A–C) Three top views (*xy* planes) for each spacer at different heights in the channel (distance from bottom): z=216, 432 and 648 μm. (D,E) Two cross-sections (*xz* planes) are shown for each spacer, at positions indicated by lines on (C). Filled and open red circles in (C) indicate the position at which the average ratios $|u_x|^2/|u|^2$ were calculated along the channel height for spacer LXS-ASD. Flow fields calculated using spacer geometries from CT scans for DOW and CON-1 at average effective velocity 0.163 m/s. (F-H, K-M) Three top views (xy planes) for each spacer at different heights in the channel (distance from bottom): z=216, 432 and 648 μm. (I,J,N,O) Two cross-sections (xz planes) are shown for each spacer, at positions indicated by lines on (H) and (M).

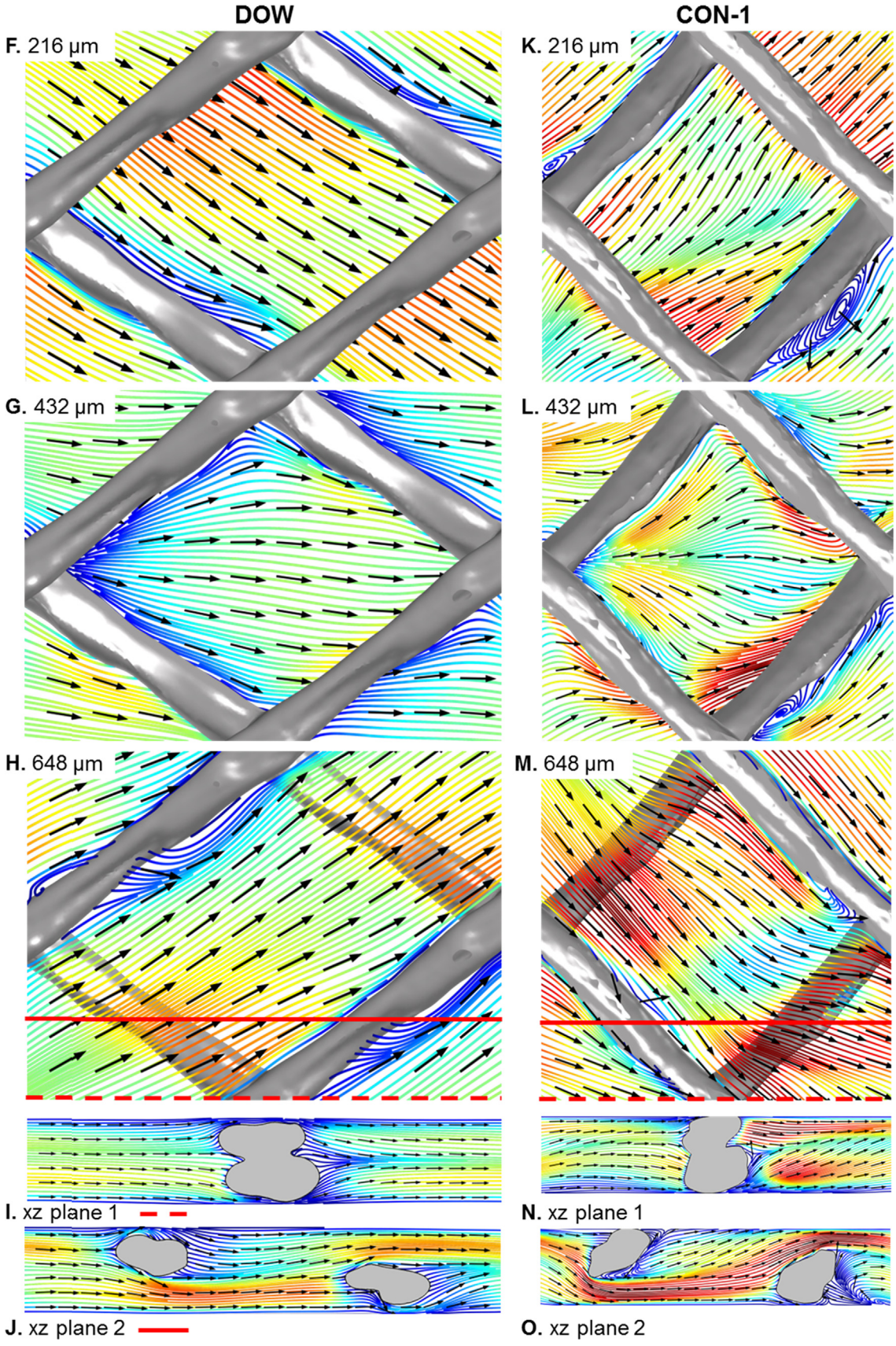

Fig. 8. (*continued*)

3.2.5. Analysis of simplified model geometries

In order to assess the importance of using for CFD an accurate geometry obtained from the CT scans, calculations were compared for spacers HYD, DOW and LXS-ASD with those obtained using simplified spacer geometries (see Fig. S2). The simplified geometries were constructed using data from the CT scans, but only viewed from the top (*xy* plane) as if obtained by microscopy. Strands with circular cross-sections but varying diameter were in this way created, with geometric characteristics based on data in Table 2.

The pressure drop for simplified spacer geometries calculated at 0.163 m/s average effective velocity is shown in Fig. 3. When comparing this simplification strategy with cylindrical strands to calculations using accurate CT scans, the difference in the calculated pressure drop depends on the amount of eccentricity of the spacer strands. For the DOW spacer the error is relatively small (14%) since the spacer strand cross-sections are rather circular, while for HYD and LXS-ASD the deviations are much larger (43% and 61%, respectively) due to the greater strand eccentricities. Based on these results, it is clear that assuming circular strand cross-sections (even of variable diameter) results in a too large simplification. The CT scan thus allows for a more accurate quantitative match to experimental data in terms of pressure drop, while decreasing the additional human bias introduced upon spacer geometry simplification.

4. Discussion

4.1. Feed channel spacer geometry

The aim of this study was too find a methodology for obtaining an accurate three-dimensional representation of feed channel spacer geometries and to evaluate its effects on the numerical modelling of a spacer's hydraulic performance. Various spacer designs have been proposed and evaluated numerically in 3-D CFD simulations [11,20,22,23,32,46,47]. However, the most studied spacer designs in silico were constructed from cylindrical strands [2] or strands with a circular cross-section with varying diameter [34,37,48] as resulted from SEM images [35]. X-ray computed tomography used in the present study revealed much more detailed feed spacer geometries than the simplified ones frequently used to model hydrodynamics and mass transfer. In general, feed spacer strands assessed in this study turned out to be rather irregularly shaped, with cross-sections more or less elliptical and also differing in orientation with respect to the main flow direction. Since the X-ray imaging is nowadays a well-established procedure, future 3-D modelling studies should be performed using geometries obtained from CT scans, or from other 3-D imaging modalities able to capture the required spatial detail.

4.2. Pressure drop measurements compared to model solutions using CT scans

The calculated values for the pressure drop using the CT scan spacer geometries were in agreement with the values measured using a flow cell to a varying extent depending on the spacer. Errors in the geometry representation yielded a systematic overestimation of the pressure drop for spacers CON-1 and DOW, while the same holds for spacers HYD and LXS-ASD to a lesser extent (Fig. 4). Comparison of experimental and model results for spacer CON-2 revealed an increasing deviation for an increasing effective velocity above 0.14 m/s. Moreover, differences in slopes between the graphs of experimental and model results depicting the friction factor as a function of the Reynolds number (Fig. 5) could indicate the onset of unsteady flow phenomena for all spacers. Santos et al. [22] reported the transition of steady to unsteady flow using ladder shaped spacers using a flow attack angle of 90° for $100 < Re < 300$. Furthermore, Shakaib et al. [33] calculated that onset of unsteady flow takes place between $150 < Re < 175$ for a flow attack angle of 45° and an L_m/h ratio of 4.25 using cylindrical filaments. The latter is comparable to the spacers evaluated in this study (ranging from 4.5 to 5.6, see Table 2). A recent experimental study by Bucs et al. [34] employing particle image velocimetry measured a deviation of 10% from the mean pressure drop for a spacer geometry similar to HYD for $Re = 160$, confirming these modelling results. Based on these studies, the onset of unsteady flow most likely caused the observed differences in experimental and model results for $125 < Re < 200$ reported in this study.

4.3. Friction due to strand shape and orientation

Schock and Miquel [12] derived an empirical correlation for the Darcy friction factor f as a function of Reynolds number, from experiments performed on several spacer types used in industrial spiral-wound membrane elements for reverse osmosis. We compared the experimental and numerical results from the present study with the correlation of Schock and Miquel, $f = 6.23 \cdot Re^{-0.3}$ (Fig. 5). All the spacers tested in this study provided a friction factor equal or higher than the one from this correlation. Notably, spacers CON-1 and CON-2 do not line up with the Schock and Miquel correlation, yielding friction factors as high as double (for $Re > 100$). A likely explanation for the observed differences is that the proposed relation was based on friction factor calculations using cylindrical spacer strand approximation and less accurate geometry dimensions than those obtained from the CT scans. Furthermore, solutions obtained from a 3-D model using a simplified geometry with cylindrical strands ($L_m/h = 4$, $d_{sp}/h = 0.5$, $\alpha = 45°$, $\beta = 90°$) for $10 < Re < 200$ (Fig. 5) showed good agreement with the trend of the model solutions obtained in this work, although the actual *f-Re* relation differs for each spacer geometry. One can therefore conclude that the established *f-Re* correlation from Schock and Miquel [12] cannot describe all mesh-type feed spacer geometries, which is in line with conclusions from [49] based on strand angle. Therefore, new spacer designs should be assessed individually based on accurate geometry measurements, which is in agreement with Picioreanu et al. [37].

4.4. Local membrane shear distribution

Shear stress has been studied using 3-D models utilizing CFD for the investigation of solute transport and deposition of particulate and bacterial fouling in spacer-filled channels. It has been reported that local membrane shear stress distribution and local velocity vectors are important factors determining the pattern of initial particle deposition on membranes [26,50]. Radu et al. [35] reported that the alignment of spacer strands with slightly varying thickness with respect to the flow has a large influence on the local shear stress and the resulting deposition pattern on the membrane, based on particle deposition experiments and numerical modelling. X-ray computed tomography, as shown in this work, provides the opportunity to investigate numerically the fouling patterns in a more accurate way.

4.5. Power input with respect to friction

Numerical modelling results on the hydraulic performance using simplified spacer geometries with cylindrical strands were compiled by Fimbres-Weihs and Wiley [2]. The power input in the form of Pn function of Re (such that $Pn = C \cdot Re^n$) was compared with results from the current study (Fig. 7**B**). All the spacers with an internal strand angle of 90° and a flow attack angle of 45°

evaluated by CT scans presented, for the same *Re*, a *Pn* well in agreement for *Re* up to 200 [26] or less than one order of magnitude larger for $100 < Re < 200$ [32] to that obtained with simplified cylindrical geometries (CON-1, CON-2, HYD and LXS-ASD). Furthermore, spacer DOW ($\beta = 70°$) showed an almost identical *Pn-Re* relation. However, the dimensionless ratio of the mesh length over the channel height, L_m/h, was 4 for the simplified cylindrical filaments while geometry characteristics extracted from CT scans in this work yielded ratios larger for all spacers (ranging from 4.5 to 5.6, see Table 2), resulting in a larger void space in a feed channel. Despite these differences in strand alignment, the comparison shows that the use of cylindrical strands yields a *Pn-Re* relation that is in good agreement with the results obtained in this work using accurate geometries. Still, the geometry representations obtained from CT scans allows one to study the local hydrodynamic effects as well without the bias introduced when constructing simplified geometries.

Additionally, the variation in exponent *n* of the *Re* number in the power relation is, although in similar range) less for the CT scanned spacer geometries (2.3–2.43) compared to the one reported for the simplified geometries (2.25–2.83), indicating a smaller increase in average velocity encountered upon increasing power input. The differences in *n* found for the five CT scanned spacer geometries further underline the conclusion by Fimbres-Weihs and Wiley [2] that the choice of a spacer depends on the flow conditions expected to be encountered and no spacer design is optimal for all possible operating conditions.

4.6. Spatial velocity distribution

The zig-zag flow pattern calculated for spacers HYD, CON-1, CON-2 and DOW at $\bar{u}_{eff} = 0.163$ m/s (shown in Fig. 8 and Fig. S4) has been experimentally observed by Da Costa et al. [3] and in earlier numerical work [26,27,37,51]. Recently, this was also experimentally measured using particle image velocimetry [34]. In other work it was found that, as the parallel strand distance L_{sp} decreases for the same channel height, flow increasingly aligns with the strands until there is very little transition between the top and bottom layers [33]. When all spacers with an internal strand angle of 90° are ranked based on their average parallel strand distance (see Table 2), the obtained ranking matches the order obtained when ranking the same spacers based on the average of the ratio $|u_x|^2/|\mathbf{u}|^2$ (ASD = 0.80, HYD = 0.76, CON-2 = 0.70, CON-1 = 0.53) for the whole computational domain. Moreover, this tendency was shown to decrease for a smaller inner strand angle, such as for spacer DOW (inner strand angle of 70°), were $|u_x|^2/|\mathbf{u}|^2$ was 0.82 in the middle of a spacer frame element. In conclusion, flow pattern characteristics found in modelling studies using simplified spacer geometries are in good agreement with the model solutions reported in this work for commercially available feed spacers used in practice.

4.7. Mechanical deformation and membrane imprinting

Matching the modelling parameters to the exact physical properties of the object under study is crucial when model solutions are translated into strategies for improving the design of that object (here, the industrial feed channel spacers). It is clear that using CT scanned spacer geometries greatly improves the quality of CFD model solutions when striving towards more quantitatively accurate results. Although it was shown in earlier work that a flat flow cell could be used to study the hydrodynamics of feed channels in spiral-wound membrane modules [12], it is difficult to reproduce the physical force exerted on spacer sheets in such a module, the subsequent deformation of the spacer and the level of membrane imprint. Furthermore, it is not yet established how to model the spacer deformation when constructing the computational domain for CFD. The area surrounding the place where the spacer is pressed into the membrane influences the flow pattern and thus affects the concentration polarization and permeation [7]. These, in turn, influence scaling and (bio)fouling processes [9]. Thus, we believe that further studies should evaluate the effect of mechanical deformations and spacer-membrane imprints on the accuracy of model predictions.

4.8. Further studies

CFD modelling was successful in matching experimental pressure drop measurements using CT scans without the bias introduced when using simplified geometries constructed from 2-D measurements. In addition, the micro-velocimetry measurements (Bucs et al., 2015) could be better matched with the velocity field calculated with CT scanned geometries. Based on the calculated flow pattern, modelling particle deposition in conjunction with experimental work (as described by Radu et al. [35], would harness the potential of using CT scanning to model (bio)fouling initiation for a given spacer design. This could improve the particle deposition model predictions presented in Radu et al. [35]. The spacer not only determines the flow pattern but also serves as a surface for initiation and subsequent fouling development. Since the position of foulant deposits affects the local rate of solute transport, this would allow a better estimation of the decline in process performance due to fouling. Therefore, simulations using the 3-D representation of a spacer geometry obtained from a CT scan should be used for accurate modelling of the solute mass transport in spacer filled channels [52].

Finally, more attention should be paid to the statistical treatment of the scanned geometries. In this work we extracted several (at least 5) spacer frames from each scanned spacer, performed CFD simulations for all these frames and then reported the average results with corresponding deviations. However, other possible approaches can be taken. A statistically adequate number of 3-D scans could be obtained (eventually from different fabrication batches), from which a “representative average shape” could be created. Even better, with an increased computational power, simulations over larger spacer patches should be performed, leading in principle to more representative results.

5. Conclusions

This study developed a method to obtain accurate three-dimensional (3-D) geometry representations for any given spacer design from X-ray computed tomography (CT) scans. Model solutions obtained using these geometries and experimental measurements led to the following conclusions:

- The CT scanning revealed that the filaments of several industrial spacers have a highly variable cross-section size and shape, which has not been addressed in fluid dynamics models until now.
- The advantage of using CT scanned spacer geometries in hydrodynamic calculations is that less bias is introduced compared to the use of conventional circular cross-section strand representations.
- Computational fluid dynamics (CFD) on four commercially available feed spacers and one new spacer with geometries from CT scans were in close agreement with experimental pressure drop measurements, for flow velocities up to 0.2 m/s as used in industrial reverse osmosis membrane operations.
- The simple cylindrical description of spacer filaments is still a

good approximation for overall hydrodynamic design of spiral-wound membrane modules. However, by providing detailed insight on the spacer filament shape, CT scans allow better quantification of local distribution of velocity and shear, possibly leading to more accurate estimations of fouling and concentration polarization.

- A newly-proposed spacer geometry with alternating strand thickness was tested (LXS-ASD), which led to lower pressure drop while being highly efficient in converting the pumping power into membrane shear. This shows that although the form drag is inevitable, the design of spacers should focus on directing flow toward the membrane while minimizing drag and generating high shear at the membrane surface.

Acknowledgements

The spacer CT scans were performed by Wim Verwaal and Joost van Meel at the Faculty of Civil Engineering and Geosciences from Delft University of Technology. We thank Thomas Lippert from Technical University of Munich, Germany, for fruitful discussions on the CFD meshing strategies. We also acknowledge Victor Koppejan from the Delft University of Technology for insightful ideas on measures to compare hydrodynamic efficiency. This research was supported by funding from King Abdullah University of Science and Technology (KAUST) and Delft University of Technology.

Appendix A. Supporting information

Supplementary data associated with this article can be found in the online version at http://dx.doi.org/10.1016/j.memsci.2016.09.005.

References

[1] K.P. Lee, T.C. Arnot, D. Mattia, A review of reverse osmosis membrane materials for desalination—development to date and future potential, J. Membr. Sci. 370 (2011) 1–22, http://dx.doi.org/10.1016/j.memsci.2010.12.036.
[2] G.A. Fimbres-Weihs, D.E. Wiley, Review of 3D CFD modeling of flow and mass transfer in narrow spacer-filled channels in membrane modules, Chem. Eng. Process. Process. Intensif. 49 (2010) 759–781, http://dx.doi.org/10.1016/j.cep.2010.01.007.
[3] A.R. Da Costa, A.G. Fane, D.E. Wiley, Spacer characterization and pressure drop modelling in spacer-filled channels for ultrafiltration, J. Membr. Sci. 87 (1994) 79–98, http://dx.doi.org/10.1016/0376-7388(93)E0076-P.
[4] In. Seok Kang, Ho. Nam Chang, The effect of turbulence promoters on mass transfer—numerical analysis and flow visualization, Int. J. Heat. Mass Transf. 25 (1982) 1167–1181, http://dx.doi.org/10.1016/0017-9310(82)90211-3.
[5] A.I. Radu, L. Bergwerff, M.C.M. van Loosdrecht, C. Picioreanu, A two-dimensional mechanistic model for scaling in spiral wound membrane systems, Chem. Eng. J. 241 (2014) 77–91, http://dx.doi.org/10.1016/j.cej.2013.12.021.
[6] S.S. Bucs, A.I. Radu, V. Lavric, J.S. Vrouwenvelder, C. Picioreanu, Effect of different commercial feed spacers on biofouling of reverse osmosis membrane systems: a numerical study, Desalination 343 (2014) 26–37, http://dx.doi.org/10.1016/j.desal.2013.11.007.
[7] A.I. Radu, J.S. Vrouwenvelder, M.C.M. van Loosdrecht, C. Picioreanu, Modeling the effect of biofilm formation on reverse osmosis performance: flux, feed channel pressure drop and solute passage, J. Membr. Sci. 365 (2010) 1–15, http://dx.doi.org/10.1016/j.memsci.2010.07.036.
[8] J.S. Vrouwenvelder, D.A. Graf von der Schulenburg, J.C. Kruithof, M.L. Johns, M. C.M. van Loosdrecht, Biofouling of spiral-wound nanofiltration and reverse osmosis membranes: a feed spacer problem, Water Res. 43 (2009) 583–594, http://dx.doi.org/10.1016/j.watres.2008.11.019.
[9] A.I. Radu, L. Bergwerff, M.C.M. van Loosdrecht, C. Picioreanu, Combined biofouling and scaling in membrane feed channels: a new modeling approach, Biofouling 31 (2015) 83–100, http://dx.doi.org/10.1080/08927014.2014.996750.
[10] D.E. Wiley, D.F. Fletcher, Techniques for computational fluid dynamics modelling of flow in membrane channels, J. Membr. Sci. 211 (2003) 127–137, http://dx.doi.org/10.1016/S0376-7388(02)00412-X.
[11] V.V. Ranade, A. Kumar, Fluid dynamics of spacer filled rectangular and curvilinear channels, J. Membr. Sci. 271 (2006) 1–15, http://dx.doi.org/10.1016/j.memsci.2005.07.013.
[12] G. Schock, A. Miquel, Mass transfer and pressure loss in spiral wound modules, Desalination 64 (1987) 339–352, http://dx.doi.org/10.1016/0011-9164(87)90107-X.
[13] J. Schwinge, D.E. Wiley, D.F. Fletcher, Simulation of the flow around spacer filaments between narrow channel walls. 1. Hydrodynamics, Ind. Eng. Chem. Res. 41 (2002) 2977–2987, http://dx.doi.org/10.1021/ie010588y.
[14] Z. Cao, D.E. Wiley, A.G. Fane, CFD simulations of net-type turbulence promoters in a narrow channel, J. Membr. Sci. 185 (2001) 157–176, http://dx.doi.org/10.1016/S0376-7388(00)00643-8.
[15] G.A. Fimbres-Weihs, D.E. Wiley, D.F. Fletcher, Unsteady flows with mass transfer in narrow zigzag spacer-filled channels: a numerical study, Ind. Eng. Chem. Res. 45 (2006) 6594–6603, http://dx.doi.org/10.1021/ie060243l.
[16] J. Schwinge, D.E. Wiley, D.F. Fletcher, Simulation of the flow around spacer filaments between channel walls. 2. Mass-transfer enhancement, Ind. Eng. Chem. Res. 41 (2002) 4879–4888, http://dx.doi.org/10.1021/ie011015o.
[17] J. Schwinge, D.E. Wiley, D.F. Fletcher, Simulation of unsteady flow and vortex shedding for narrow spacer-filled channels, Ind. Eng. Chem. Res. 42 (2003) 4962–4977, http://dx.doi.org/10.1021/ie030211n.
[18] K.J. Martin, C. Picioreanu, R. Nerenberg, Multidimensional modeling of biofilm development and fluid dynamics in a hydrogen-based, membrane biofilm reactor (MBfR), Water Res 47 (2013) 4739–4751, http://dx.doi.org/10.1016/j.watres.2013.04.031.
[19] A.L. Ahmad, K.K. Lau, M.Z. Abu Bakar, Impact of different spacer filament geometries on concentration polarization control in narrow membrane channel, J. Membr. Sci. 262 (2005) 138–152, http://dx.doi.org/10.1016/j.memsci.2005.06.056.
[20] J. Liu, Z. Liu, X. Xu, F. Liu, Saw-tooth spacer for membrane filtration: hydrodynamic investigation by PIV and filtration experiment validation, Chem. Eng. Process. Process. Intensif. 91 (2015) 23–34, http://dx.doi.org/10.1016/j.cep.2015.03.013.
[21] P. Sousa, A. Soares, E. Monteiro, A. Rouboa, A. CFD, study of the hydrodynamics in a desalination membrane filled with spacers, Desalination 349 (2014) 22–30, http://dx.doi.org/10.1016/j.desal.2014.06.019.
[22] J.L.C. Santos, V. Geraldes, S. Velizarov, J.G. Crespo, Investigation of flow patterns and mass transfer in membrane module channels filled with flow-aligned spacers using computational fluid dynamics (CFD), J. Membr. Sci. 305 (2007) 103–117, http://dx.doi.org/10.1016/j.memsci.2007.07.036.
[23] F. Li, W. Meindersma, A.B. de Haan, T. Reith, Novel spacers for mass transfer enhancement in membrane separations, J. Membr. Sci. 253 (2005) 1–12, http://dx.doi.org/10.1016/j.memsci.2004.12.019.
[24] J. Schwinge, D.E. Wiley, A.G. Fane, Novel spacer design improves observed flux, J. Membr. Sci. 229 (2004) 53–61, http://dx.doi.org/10.1016/j.memsci.2003.09.015.
[25] I.S. Ngene, R.G.H. Lammertink, M. Wessling, W.G.J. Van der Meer, Particle deposition and biofilm formation on microstructured membranes, J. Membr. Sci. 364 (2010) 43–51, http://dx.doi.org/10.1016/j.memsci.2010.07.048.
[26] G.A. Fimbres-Weihs, D.E. Wiley, Numerical study of mass transfer in three-dimensional spacer-filled narrow channels with steady flow, J. Membr. Sci. 306 (2007) 228–243, http://dx.doi.org/10.1016/j.memsci.2007.08.043.
[27] S.K. Karode, A. Kumar, Flow visualization through spacer filled channels by computational fluid dynamics I.: pressure drop and shear rate calculations for flat sheet geometry, J. Membr. Sci. 193 (2001) 69–84, http://dx.doi.org/10.1016/S0376-7388(01)00494-X.
[28] C.P. Koutsou, S.G. Yiantsios, A.J. Karabelas, Direct numerical simulation of flow in spacer-filled channels: Effect of spacer geometrical characteristics, J. Membr. Sci. 291 (2007) 53–69, http://dx.doi.org/10.1016/j.memsci.2006.12.032.
[29] C.P. Koutsou, S.G. Yiantsios, A.J. Karabelas, Numerical simulation of the flow in a plane-channel containing a periodic array of cylindrical turbulence promoters, J. Membr. Sci. 231 (2004) 81–90, http://dx.doi.org/10.1016/j.memsci.2003.11.005.
[30] K.K. Lau, M.Z. Abu Bakar, A.L. Ahmad, T. Murugesan, Feed spacer mesh angle: 3D modeling, simulation and optimization based on unsteady hydrodynamic in spiral wound membrane channel, J. Membr. Sci. 343 (2009) 16–33, http://dx.doi.org/10.1016/j.memsci.2009.07.001.
[31] F. Li, G.W. Meindersma, A.B. de Haan, T. Reith, Optimization of non-woven spacers by CFD and validation by experiments, Desalination 146 (2002) 209–212, http://dx.doi.org/10.1016/S0011-9164(02)00472-1.
[32] F. Li, W. Meindersma, A.B. de Haan, T. Reith, Optimization of commercial net spacers in spiral wound membrane modules, J. Membr. Sci. 208 (2002) 289–302, http://dx.doi.org/10.1016/S0376-7388(02)00307-1.
[33] M. Shakaib, S.M.F. Hasani, M. Mahmood, Study on the effects of spacer geometry in membrane feed channels using three-dimensional computational flow modeling, J. Membr. Sci. 297 (2007) 74–89, http://dx.doi.org/10.1016/j.memsci.2007.03.010.
[34] S.S. Bucs, R. Valladares Linares, J.O. Marston, A.I. Radu, J.S. Vrouwenvelder, C. Picioreanu, Experimental and numerical characterization of the water flow in spacer-filled channels of spiral-wound membranes, Water Res. 87 (2015) 299–310, http://dx.doi.org/10.1016/j.watres.2015.09.036.
[35] A.I. Radu, M.S.H. van Steen, J.S. Vrouwenvelder, M.C.M. van Loosdrecht, C. Picioreanu, Spacer geometry and particle deposition in spiral wound membrane feed channels, Water Res. 64 (2014) 160–176, http://dx.doi.org/10.1016/j.watres.2014.06.040.
[36] S. West, M. Wagner, C. Engelke, H. Horn, Optical coherence tomography for the in situ three-dimensional visualization and quantification of feed spacer channel fouling in reverse osmosis membrane modules, J. Membr. Sci. 498 (2016) 345–352, http://dx.doi.org/10.1016/j.memsci.2015.09.047.

[37] C. Picioreanu, J.S. Vrouwenvelder, M.C.M. van Loosdrecht, Three-dimensional modeling of biofouling and fluid dynamics in feed spacer channels of membrane devices, J. Membr. Sci. 345 (2009) 340–354, http://dx.doi.org/10.1016/j.memsci.2009.09.024.
[38] A. Siddiqui, N. Farhat, S.S. Bucs, R.V. Linares, C. Picioreanu, J.C. Kruithof, M.C. M. van Loosdrecht, J. Kidwell, J.S. Vrouwenvelder, Development and characterization of 3D-printed feed spacers for spiral wound membrane systems, Water Res. 91 (2016) 55–67, http://dx.doi.org/10.1016/j.watres.2015.12.052.
[39] G.T. Herman, Fundamentals of Computerized Tomography, Springer, London, 2009, http://link.springer.com/10(0.1007/978-1-84628)-723-7 (accessed 30.03.16)..
[40] P.J. Roache, Perspective: a method for uniform reporting of grid refinement studies, J. Fluids Eng. 116 (1994) 405–413, http://dx.doi.org/10.1115/1.2910291.
[41] J.S. Vrouwenvelder, C. Hinrichs, W.G.J. Van der Meer, M.C.M. Van Loosdrecht, J. C. Kruithof, Pressure drop increase by biofilm accumulation in spiral wound RO and NF membrane systems: role of substrate concentration, flow velocity, substrate load and flow direction, Biofouling 25 (2009) 543–555, http://dx.doi.org/10.1080/08927010902972225.
[42] J.S. Vrouwenvelder, J.A.M. van Paassen, L.P. Wessels, A.F. van Dam, S.M. Bakker, The membrane fouling simulator: a practical tool for fouling prediction and control, J. Membr. Sci. 281 (2006) 316–324, http://dx.doi.org/10.1016/j.memsci.2006.03.046.
[43] J.S. Vrouwenvelder, J.A.M. van Paassen, J.C. Kruithof, M.C.M. van Loosdrecht, Sensitive pressure drop measurements of individual lead membrane elements for accurate early biofouling detection, J. Membr. Sci. 338 (2009) 92–99, http://dx.doi.org/10.1016/j.memsci.2009.04.016.
[44] S.S. Bucs, N. Farhat, A. Siddiqui, R.V. Linares, A. Radu, J.C. Kruithof, J. S. Vrouwenvelder, Development of a setup to enable stable and accurate flow conditions for membrane biofouling studies, Desalin. Water Treat. 57 (2016) 12893–12901, http://dx.doi.org/10.1080/19443994.2015.1057037.
[45] P.A. Araújo, J.C. Kruithof, M.C.M. Van Loosdrecht, J.S. Vrouwenvelder, The potential of standard and modified feed spacers for biofouling control, J. Membr. Sci. 403–404 (2012) 58–70, http://dx.doi.org/10.1016/j.memsci.2012.02.015.
[46] D. Dendukuri, S.K. Karode, A. Kumar, Flow visualization through spacer filled channels by computational fluid dynamics-II: improved feed spacer designs, J. Membr. Sci. 249 (2005) 41–49, http://dx.doi.org/10.1016/j.memsci.2004.06.062.
[47] C.P. Koutsou, A.J. Karabelas, A novel retentate spacer geometry for improved spiral wound membrane (SWM) module performance, J. Membr. Sci. 488 (2015) 129–142, http://dx.doi.org/10.1016/j.memsci.2015.03.064.
[48] J.S. Vrouwenvelder, C. Picioreanu, J.C. Kruithof, M.C.M. van Loosdrecht, Biofouling in spiral wound membrane systems: three-dimensional CFD model based evaluation of experimental data, J. Membr. Sci. 346 (2010) 71–85, http://dx.doi.org/10.1016/j.memsci.2009.09.025.
[49] A.R. Da Costa, A.G. Fane, C.J.D. Fell, A.C.M. Franken, Optimal channel spacer design for ultrafiltration, J. Membr. Sci. 62 (1991) 275–291, http://dx.doi.org/10.1016/0376-7388(91)80043-6.
[50] Y.-L. Li, K.-L. Tung, Y.-S. Chen, K.-J. Hwang, CFD analysis of the initial stages of particle deposition in spiral-wound membrane modules, Desalination 287 (2012) 200–208, http://dx.doi.org/10.1016/j.desal.2011.10.001.
[51] M. Shakaib, S.M.F. Hasani, M. Mahmood, CFD modeling for flow and mass transfer in spacer-obstructed membrane feed channels, J. Membr. Sci. 326 (2009) 270–284, http://dx.doi.org/10.1016/j.memsci.2008.09.052.
[52] N. Horstmeyer, T. Lippert, C. Picioreanu, J. Prša, J. Drewes, Impact of geometric accuracy of spacer models on reliability of CFD simulations on membrane feed channels, Submitted to Separation and Purification Technology.

Web references

[WR1] STL File Format – ⟨https://en.wikipedia.org/wiki/STL_(file_format)⟩.
[WR2] Iso2Mesh Toolbox for MATLAB – ⟨http://iso2mesh.sourceforge.net/cgi-bin/index.cgi⟩.
[WR3] MeshLab – ⟨http://meshlab.sourceforge.net/⟩.
[WR4] netfabb Basic – ⟨http://www.netfabb.com/basic.php⟩.